

Microstructure and Mechanical Properties of Long Ti-6Al-4V Rods Additively Manufactured by Selective Electron Beam Melting Out of a Deep Powder Bed and the Effect of Subsequent Hot Isostatic Pressing



S.L. LU, H.P. TANG, Y.P. NING, N. LIU, D.H. STJOHN, and M. QIAN

An array of eight long Ti-6Al-4V rods (diameter: 12 mm; height: 300 mm) have been additively manufactured, vertically and perpendicular to the powder bed, by selective electron beam melting (SEBM). The purpose was to identify and understand the challenges of fabricating Ti-6Al-4V samples or parts from a deep powder bed (more than 200-mm deep) by SEBM and the necessity of applying post heat treatment. The resulting microstructure and mechanical properties of these Ti-6Al-4V rods were characterized along their building (*i.e.*, axial) direction by dividing each rod into three segments (top, middle, and bottom), both before (*i.e.*, as-built) and after hot isostatic pressing (HIP). The as-built microstructure of each rod was inhomogeneous; it was coarsest in the top segment, which showed a near equilibrium α - β lamellar structure, and finest in the bottom segment, which featured a non-equilibrium mixed structure. The tensile properties varied along the rod axis, especially the ductility, but all tensile properties met the requirements specified by ASTM F3001-14. HIP increased the relative density from 99.03 pct of the theoretical density (TD) to 99.90 pct TD and homogenized the microstructure thereby leading to highly consistent tensile properties along the rod axis. The temperature of the stainless steel substrate used in the powder bed was monitored. The as-built inhomogeneous microstructure is attributed to the temperature gradient in the deep powder bed. Post heat treatment is thus necessary for Ti-6Al-4V samples or parts manufactured from a deep powder bed by SEBM. This differs from the additive manufacturing of small samples or parts from a shallow powder bed (less than 100-mm deep) by SEBM.

DOI: 10.1007/s11661-015-2976-3

© The Minerals, Metals & Materials Society and ASM International 2015

I. INTRODUCTION

INTEREST in additive manufacturing (AM) of titanium (Ti) alloys continues to grow rapidly worldwide, especially for aerospace and biomedical applications.^[1–6] Although much effort has been made to establish the processing-microstructure-property relationships for additively manufactured (AMed) Ti alloys,^[7,8] there are still a number of unanswered

important questions, particularly for the AM of Ti alloy samples or parts from a deep powder bed. Two such concerns are microstructure inhomogeneity and hidden defects. They apply to the AM processes by both SEBM and selective laser melting (SLM), which are the two premier powder-bed-based metal AM processes. They are similar but differ in a number of aspects including the melting environment, requirements for powder size, preheating temperatures, and therefore the as-built microstructure, mechanical properties, and surface finish.^[3–5]

The SEBM-based AM process was first made available to the manufacturing industry by the Arcam AB Company (Sweden) in 2002.^[9] The process is particularly suited to the AM of Ti alloys due to the high vacuum building chamber used, which alleviates the pick-up of oxygen and nitrogen from the building environment during AM (the oxygen content of the used powder still increases^[3]). To date, the process has proved to be competent in the manufacturing of small Ti alloy samples or parts with excellent mechanical properties and consistency while requiring no post-AM heat treatment (which is in contrast to those AMed by SLM).^[3] As a result, it is being increasingly adopted by industry. For instance, more than 40,000 titanium acetabular cups made by the process had been

S.L. LU, Ph.D Candidate, is with the School of Materials and Metallurgy, Northeastern University, Shenyang 110819, P.R. China and with the State Key Laboratory of Porous Metal Materials, Northwest Institute for Nonferrous Metal Research, Xi'an 710016, P.R. China, and also with the Centre for Advanced Materials Processing and Manufacturing, School of Mechanical and Mining Engineering, The University of Queensland, St Lucia, QLD 4072, Australia. H.P. TANG, Professor, Y.P. NING, Graduate Student, and N. LIU, Junior Engineer, are with the State Key Laboratory of Porous Metal Materials, Northwest Institute for Nonferrous Metal Research. Contact e-mail: thpfys@126.com D.H. STJOHN, Professor, is with the Centre for Advanced Materials Processing and Manufacturing, School of Mechanical and Mining Engineering, The University of Queensland. M. QIAN, Professor, is with the Centre for Additive Manufacturing, School of Aerospace, Mechanical and Manufacturing Engineering, RMIT University, Melbourne, VIC 3001, Australia. Contact e-mail: ma.qian@rmit.edu.au

Manuscript submitted March 3, 2015.

Article published online May 30, 2015

implanted by April 2014 and globally this accounts for about 2 pct of the production of acetabular cups.^[10] However, what is missing from a research perspective is that, to the authors' knowledge, no studies have been published as yet on the microstructure-property relationships of long Ti alloy samples or parts AMed by SEBM, while there are clear industry demands for the AM of such parts. The reason behind this could be the high cost of pursuing such studies or the lack of communications of research data from those who have carried out the studies. Either way this affects the development of a comprehensive understanding of the SEBM-based AM process for Ti alloys and other metals too.

This study aims to fill this gap in the literature on the AM of Ti alloys by SEBM. For this reason, a commercial Arcam A2 system was used, which allows a maximum building height of 350 mm. An array of eight 300 mm Ti-6Al-4V rods were vertically built, and their microstructure and mechanical properties were investigated in detail along their building (*i.e.*, the axial) direction both in the as-built state and after hot isostatic pressing (HIP).

II. EXPERIMENTAL PROCEDURE

A. Materials and Manufacturing

Virgin extra low interstitial (ELI) Arcam Ti-6Al-4V spherical powder was used and its composition is listed in Table I, which meets the requirements of ASTM F3001-14.^[11] Figure 1 shows the selected size-range distribution of the powder, which exhibits two peak size ranges from 53 to 63 and 75 to 90 μm .

All samples were built using an Arcam A2 system (voltage: 60 kV; beam power: 50 to 3500 W, which can be varied continuously) and the AM parameters utilized are summarized in Table II (no changes during the AM process). An array of eight Ti-6Al-4V rods, each measuring 300 mm in height and 12 mm in diameter, was manufactured in one batch along with the AM of a 300 mm high Ti-6Al-4V component. Figure 2(a) shows the schematic layout of these rods and the part in the powder bed which uses a stainless steel substrate (210 mm \times 210 mm \times 10 mm) at the bottom. Two as-built long Ti-6Al-4V rods are shown in Figure 2(b). The temperature of the stainless steel substrate during AM was monitored through a thermal couple attached to the bottom of substrate and the recorded temperature profile is shown in Figure 2(c). It started from 1003 K (730 $^{\circ}\text{C}$)

(a pre-set preheating temperature) and declined progressively to 633 K (360 $^{\circ}\text{C}$) over the subsequent 60 hours of AM process. The vacuum pressure in the building chamber was kept at about 2×10^{-2} Pa in the presence of helium, controlled through a system-adjusted helium gas flow (which means that the actual vacuum pressure was lower than 2×10^{-2} Pa). After AM, three rods were subjected to HIP at 1193 K (920 $^{\circ}\text{C}$) for 120 minutes under 100 MPa (proposed by Arcam AB Co.).

B. Characterization and Tensile Testing

Samples for microstructural characterization and tensile testing were cut from each rod. Figure 3(a) shows the sampling protocol along the rod axis. Three tensile specimens were machined from each rod, denoted as top, middle, and bottom, respectively. The tensile specimen dimensions prepared according to ASTM E8/E8M-11^[12] are shown in Figure 3(b). Tensile testing was conducted on an Instron tester (Model 5982, Instron Co., USA) at a strain rate of 10^{-3} s⁻¹. Each set of tensile property data was averaged from the results of three samples. Densities of samples were determined by the Archimedes method. Samples selected for metallographic examination were all cut into halves along their axial (*i.e.*, building) direction and mechanically ground and polished. They were then etched with a Kroll's reagent (2 mL HF, 4 mL HNO₃, and 94 mL H₂O) for characterization using optical microscopy and scanning electron microscopy (SEM, a Jeol 6610, JEOL Ltd. Japan, operated at 10 or 20 kV). Electron backscattered diffraction (EBSD) was conducted on well-polished

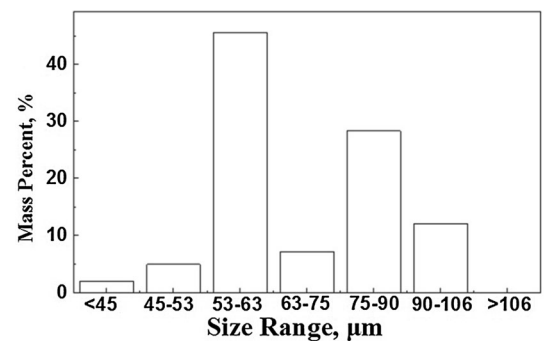


Fig. 1—Size-range distribution of the as-received virgin Arcam Ti-6Al-4V ELI powder.

Table I. Compositions of the Virgin Ti-6Al-4V Powder and the As-Built Sample

Sample Status	Composition (Wt Pct)							
	H	C	O	N	Fe	Al	V	Ti
Virgin powder	0.003	< 0.005	0.08	0.008	0.24	6.47	4.08	bal.
As-built sample	—	—	0.10	0.008	—	6.2	4.05	bal.

Table II. AM Conditions Used for the Manufacturing of the Ti-6Al-4V Rods

	Preheating			Layer Melting	
	Beam Spot Size	Beam Current	Scanning Speed	Beam Current	Scanning Speed
Electron beam	100 μm	30 mA	1 to $1.3 \times 10^4 \text{ mm s}^{-1}$	20 mA	4500 mm s^{-1}
Stainless steel substrate temperature	1003 K (730 °C)				
Powder layer thickness	50 μm				

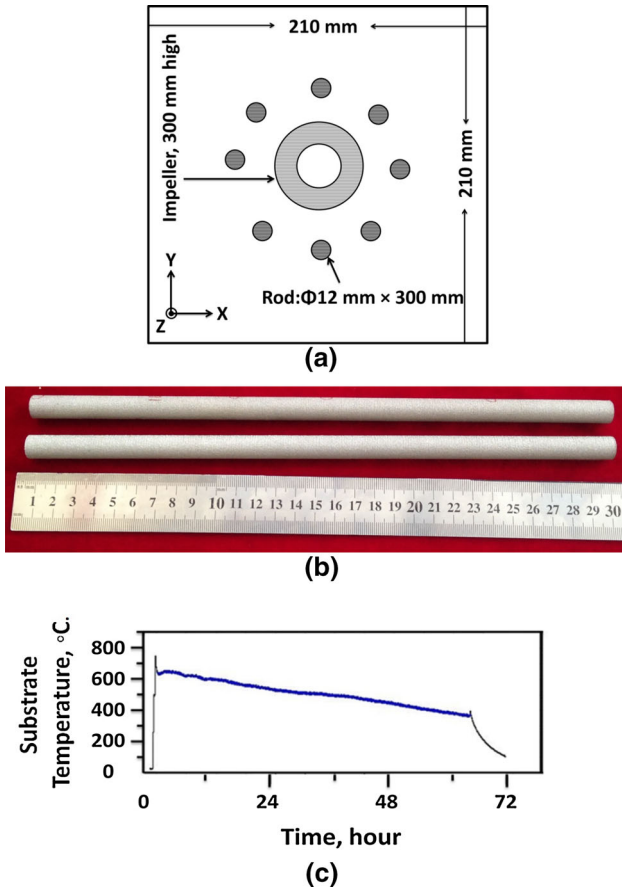


Fig. 2—(a) Schematic layout of the Ti-6Al-4V rods additively manufactured on a stainless steel substrate (210 mm \times 210 mm \times 10 mm), (b) two as-built rods by SEBM, and (c) temperature profile of the stainless steel substrate recorded during AM.

transverse sections of the rod sample (no noticeable topography was observed at magnifications up to 1000 times) using a Nova NanoSEM 230 (FEI Co., USA) at 20 kV with a step size of 20 nm. The as-polished sample surface was inclined at 70 deg with respect to the horizontal plane, while the electron beam had an incident angle of 20 deg with respect to the as-polished sample surface (the rod axis was perpendicular to the as-polished sample surface). X-ray diffraction (XRD) was conducted using a Bruker D8 Advance Diffractometer at 40 kV with a Cu K_{α} radiation (wavelength $\lambda_{k\alpha 1} = 1.54060 \text{ \AA}$).

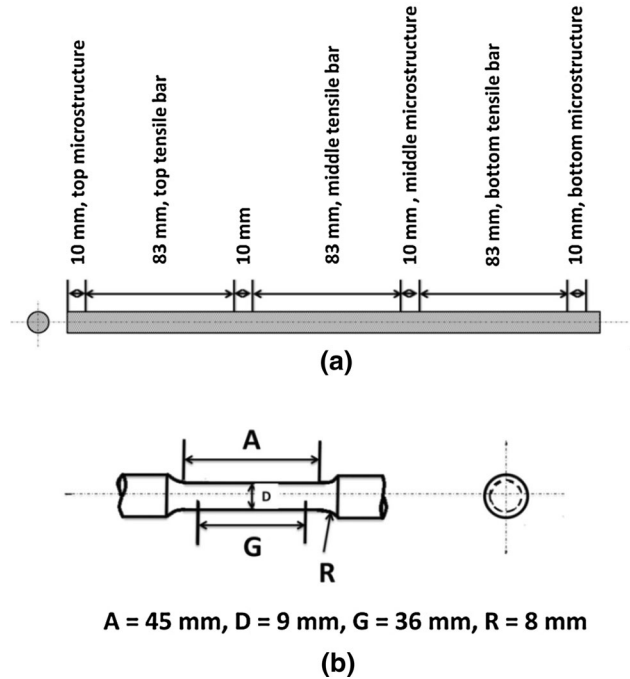


Fig. 3—(a) Protocol for sampling from the Ti-6Al-4V rod for microstructural characterization and tensile testing and (b) tensile specimen geometry and dimensions by the ASTM E8/E8M-11.

III. RESULTS AND DISCUSSION

A. Microstructure

The composition of the as-built Ti-6Al-4V rod is also listed in Table I. The oxygen content increased from 0.08 to 0.10 wt pct, while the aluminum content decreased from 6.47 to 6.20 wt pct. The vanadium content remained almost unchanged. The resulting composition meets the specification of Ti-6Al-4V according to ASTM F3001-14.^[1] Figure 4 shows the optical microstructures of the rod obtained from its top, middle, and bottom segments (see Figure 3(a)) before (*i.e.*, as-built) and after HIP. The prior- β columnar grain structure was clear throughout the rod in the as-built state as shown in Figures 4(a) through (c), and this feature was preserved after HIP at 1193 K (920 °C) in the $\alpha + \beta$ region for 120 minutes under 100 MPa (Figures 4(a') through (c')). However, HIP led to noticeable growth of both α and β lamellae.

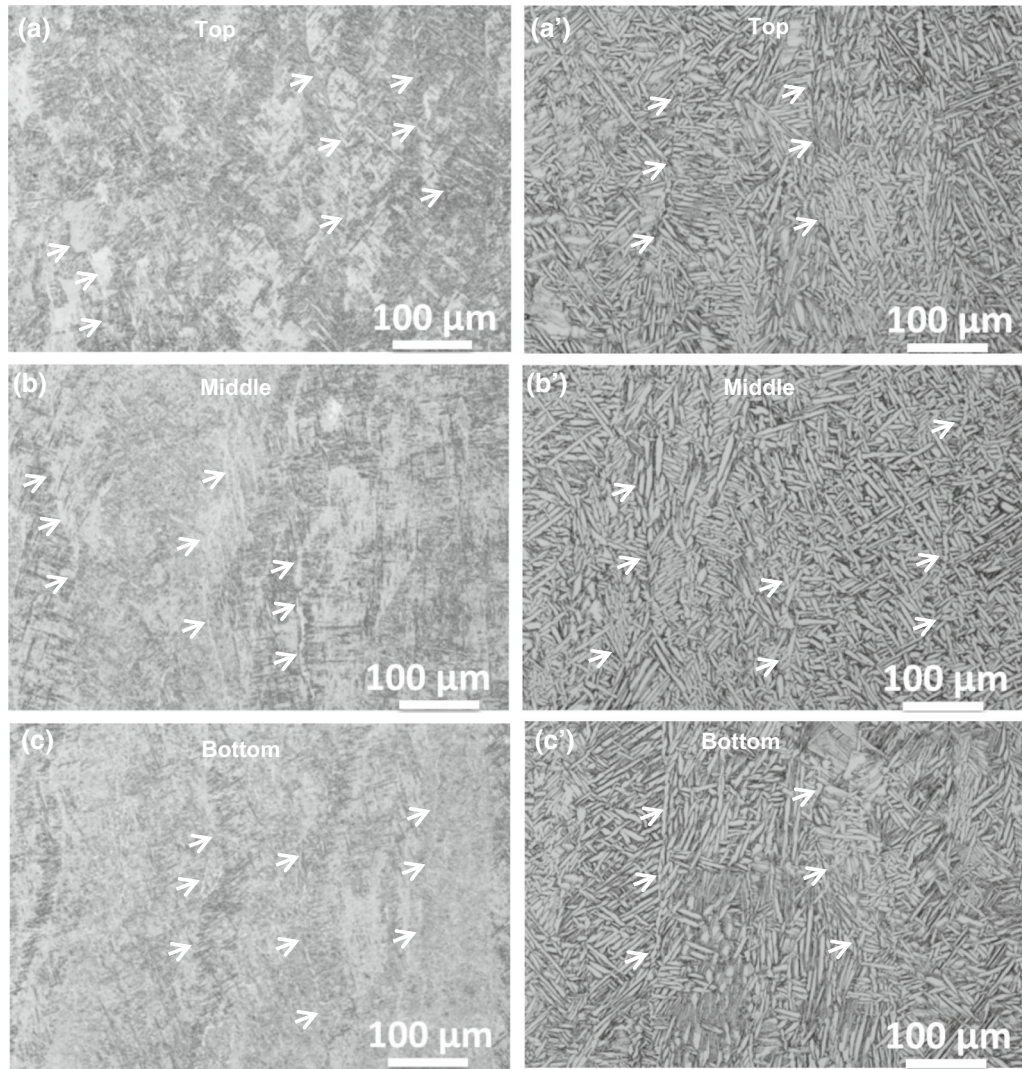


Fig. 4—Optical microstructures of the rod before (*a* through *c*) and after HIP (*a'* through *c'*) at 920 °C in the $\alpha + \beta$ region for 120 min under 100 MPa. Arrows indicate prior- β columnar grain boundaries. Refer to Fig. 3 for the top, middle, and bottom positions.

Table III. Densities of the As-Built Ti-6Al-4V Rod and After HIP (The Theoretical Density of Ti-6Al-4V is 4.430 g/cm³^[3])

Sample Status	Top (g cm ⁻³)	Middle (g cm ⁻³)	Bottom (g cm ⁻³)
As-built	4.388 ± 0.001	4.388 ± 0.005	4.388 ± 0.001
After HIP	4.426 ± 0.009	4.427 ± 0.010	4.426 ± 0.007

Table III lists the densities of the top, middle, and bottom segments of the rod before and after HIP. The top, middle, and bottom segments of the as-built rod achieved densities of 4.389 ± 0.009 g/cm³ [99.08 pct theoretical density (TD)], 4.387 ± 0.008 g/cm³ (99.03 pct TD), and 4.395 ± 0.010 g/cm³ (99.21 pct TD), respectively, vs the theoretical density 4.430 g/cm³ of Ti-6Al-4V.^[3] HIP further increased the density uniformly to 4.426 g/cm³ or 99.90 pct TD throughout the rod with no detectable statistical differences according to the Archimedes method. Another observation was

that prior to HIP there were occasionally observed gas bubbles and minor delaminated areas as shown in Figure 5 but no such defects were observed after HIP in each sample examined. The recommended HIP practice was effective in eliminating or healing such defects rendering the microstructure essentially defects free.

Figure 6 shows the SEM micrographs of the as-built Ti-6Al-4V rod from the top to the bottom. The top segment had a typical α - β lamellar structure (Figure 6(a)), while the bottom segment (Figure 6(c)) exhibited a mixed microstructure which consisted of

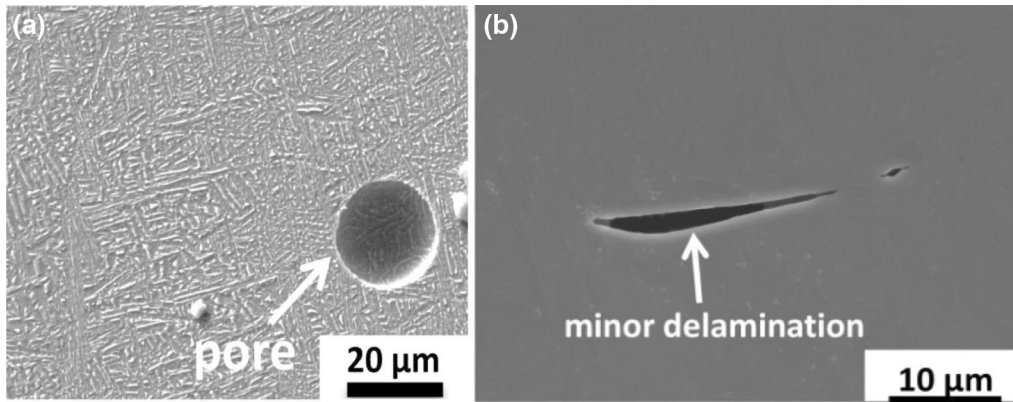


Fig. 5—Defects occasionally observed in the as-built Ti-6Al-4V rods: (a) a gas bubble and (b) minor local delamination.

portions of α - β lamellar structures and non-lamellar α - β structures with small isolated β phase particles being embedded in the α matrix. The middle segment (Figure 6(b)) fell in between but it was still largely a lamellar structure. The bottom segment showed the finest microstructure, while the top segment displayed the coarsest microstructure. For instance, the α plate thickness, measured from the SEM micrographs, decreased from $1.06 \pm 0.05 \mu\text{m}$ in the top segment to $0.92 \pm 0.02 \mu\text{m}$ in the middle segment and further to $0.74 \pm 0.06 \mu\text{m}$ in the bottom segment. The α plate thickness was determined by measuring the spacing between two neighboring β plates (the bright phase shown in Figure 6) from five selected zones in the microstructure and the average was taken. These microstructural changes will be discussed subsequently together with the EBSD observations presented below.

Figure 7 shows the EBSD results obtained from the top, middle, and bottom segments of the rod. The inverse pole figures (IPF) shown in Figures 7(a), (c), (e) indicated that the neighboring α lamellae tended to display the same color, implying that they were of the same crystalline direction relative to the sample coordinate system. This trend intensified from the top to the bottom of the long rod. The right-hand side images (Figures 7(b), (d), (f)) were phase distribution images (red for α , green for β). The β phase was distributed in different forms in the α matrix. The top, middle, and bottom segments of the rod contained about 8.8, 4.8, and 3.0 pct of the β phase (area fraction), respectively, measured from the EBSD results. Several transverse sections were examined from each segment of the rod sample and the microstructure was found to be consistent within each segment in terms of the β phase area fraction detected, although it varied from segment to segment. The area fractions of the β phase measured from each segment were thus used to approximate the volume fractions of the β phase in the respective segments. The equilibrium volume fraction of the β phase in Ti-6Al-4V is about 10 pct^[13] at room temperature. This indicates that the microstructure of the top segment of the rod is close to its equilibrium state, while the microstructures of both the middle and bottom

segments show a significant departure. This can be understood as follows.

Close to the stainless steel substrate (*i.e.*, the bottom of the powder bed), heat was conducted quickly through the substrate whose temperature kept decreasing during AM as shown in Figure 2(c). This led to a fast cooling rate at the bottom segment during both SEBM and the subsequent solid-state phase transformation. Hence the resulting microstructure was finest in the bottom segment. As the AM process went on, both the building height of the sample and the depth of the powder bed kept increasing layer by layer. However, the thermal conductivity of solid Ti-6Al-4V is notoriously small (7 vs 237 $\text{W m}^{-1} \text{K}^{-1}$ for Al^[14]) and that of the Ti-6Al-4V powder is even smaller. Consequently, the heat in the powder bed arising from the SEBM process and the subsequent latent heat release during solidification is difficult to quickly dissipate through the top and the sides of the powder bed, while the bottom is cooler due to the stainless steel substrate. This thermal gradient in the powder bed is expected to worsen beyond a certain powder bed depth. As a result, the top segment of the rod is exposed to a higher temperature environment than the bottom segment. This results in not only a slower cooling rate during solidification after SEBM but also an effectively annealed near equilibrium α - β microstructure in the top segment of the long rod. As shown in Figure 2(c), the temperature of the stainless steel substrate kept decreasing during AM. This provides a point of reference for the estimate of the temperature profile in the bottom part of the powder bed. The small presence of the β phase around 3.0 pct in the bottom segment of the rod is a strong indication that the temperature environment in the bottom part of the powder bed was inadequate to anneal the as-built Ti-6Al-4V to a near equilibrium state, which should show about 10 pct of the β phase.

Despite the noticeable difference in microstructure along the rod in the as-built state, after HIP at 1193 K (920 °C) for 120 minutes under 100 MPa, the microstructure became homogeneous from the top to the bottom. Figure 8 shows the representative microstruc-

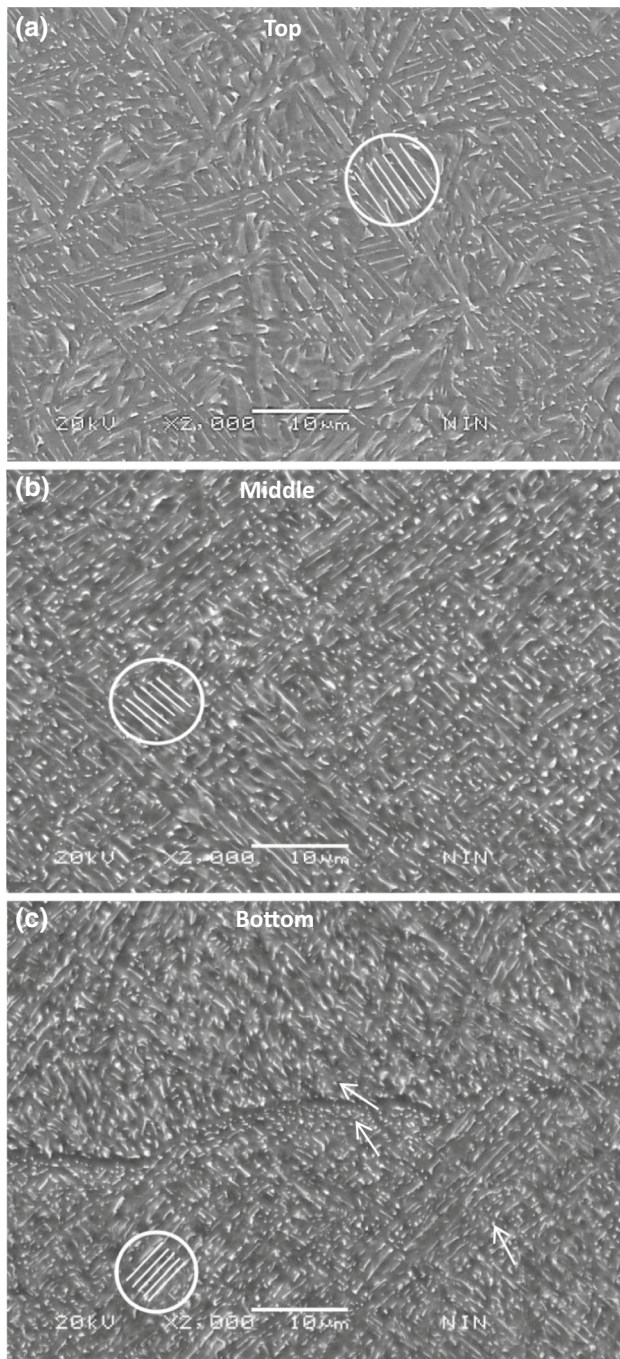


Fig. 6—SEM micrographs of the as-built Ti-6Al-4V rod: (a) top, (b) middle, and (c) bottom (see Fig. 3(a)). The bright phase is β . The bottom had the finest microstructure.

tures observed in the top and bottom segments after HIP and the EBSD mapping results of the bottom segment. The microstructure coarsened significantly after HIP. For instance, the α plate thickness grew from less than $1\ \mu\text{m}$ to about $5\ \mu\text{m}$. Another observation is that there was precipitation of secondary α plates in the retained β phase (see the inset images in Figures 8(a),

(b)), mostly notably at the triple points of the primary α plates. Such secondary α phase particles were observed in all samples after HIP. The β phase fraction after HIP was measured to be 9.5 pct, close to the equilibrium state reported in Reference 13.

Figure 9 shows the XRD spectra obtained from the top (I), middle (II), and bottom (III) segments of the as-built rod before and after HIP. Also included is the XRD spectrum for the virgin Ti-6Al-4V powder (VI). The α phase was predominant in each case as expected. However, in the as-built state, the XRD spectrum obtained from the top segment exhibited a (110) peak (see inset in Figure 9(a)), which was barely visible in the XRD spectrum obtained from the middle segment but invisible in that obtained from the bottom segment. These observations are qualitatively consistent with the EBSD results. After HIP, signals corresponding to the (110) peak are clearer and stronger (see inset in Figure 9(b)), indicative of an increase in the presence of the β phase after HIP. This is consistent with the near equilibrium α - β lamellar structure observed after HIP (Figure 8) in which the β phase volume fraction is expected to be around 10 pct compared to only about 3 pct at the bottom segment prior to HIP.

B. Tensile Properties

The tensile property and ductility results obtained from the top, middle, and bottom segments of the as-built Ti-6Al-4V rods before and after HIP are listed in Table IV. The tensile properties showed inconsistency from the top to the bottom of the rod in the as-built state, although they still meet the specifications set by ASTM F3001-14.^[11] In particular, the Reduction of Area decreased from (51.4 ± 2.4) to (33.9 ± 1.5) pct from the top to the bottom. As expected, HIP reduced tensile strengths, improved ductility, and realized highly consistent tensile properties throughout the rod. It was noted that the top segment of the as-built rod exhibited the largest tensile elongation (16.4 pct) and reduction of area (51.4 pct), which are essentially the same as their respective values obtained after HIP (see Table IV). This further indicates that the microstructure of the top segment of the rod is close to its equilibrium state. Also included in Table IV are the minimum requirements for the tensile properties of Ti-6Al-4V by ASTM F3001-14.^[11] The additively manufactured Ti-6Al-4V rod meets the minimum requirements for all tensile properties including the reduction of area both before and after HIP.

The fracture surfaces of the top, middle, and bottom segments of the rod samples before and after HIP are shown in Figure 10. Ductile fracture features were observed in each case, featured by dimples and tear ridges. After HIP, the entire rod showed very similar fracture surface characteristics (Figures 10(a') through (c')) from the top to the bottom, consistent with the similar microstructures as shown in Figures 4(a') through (c') and the similar tensile properties are listed in Table IV. The fracture surface of the top segment of

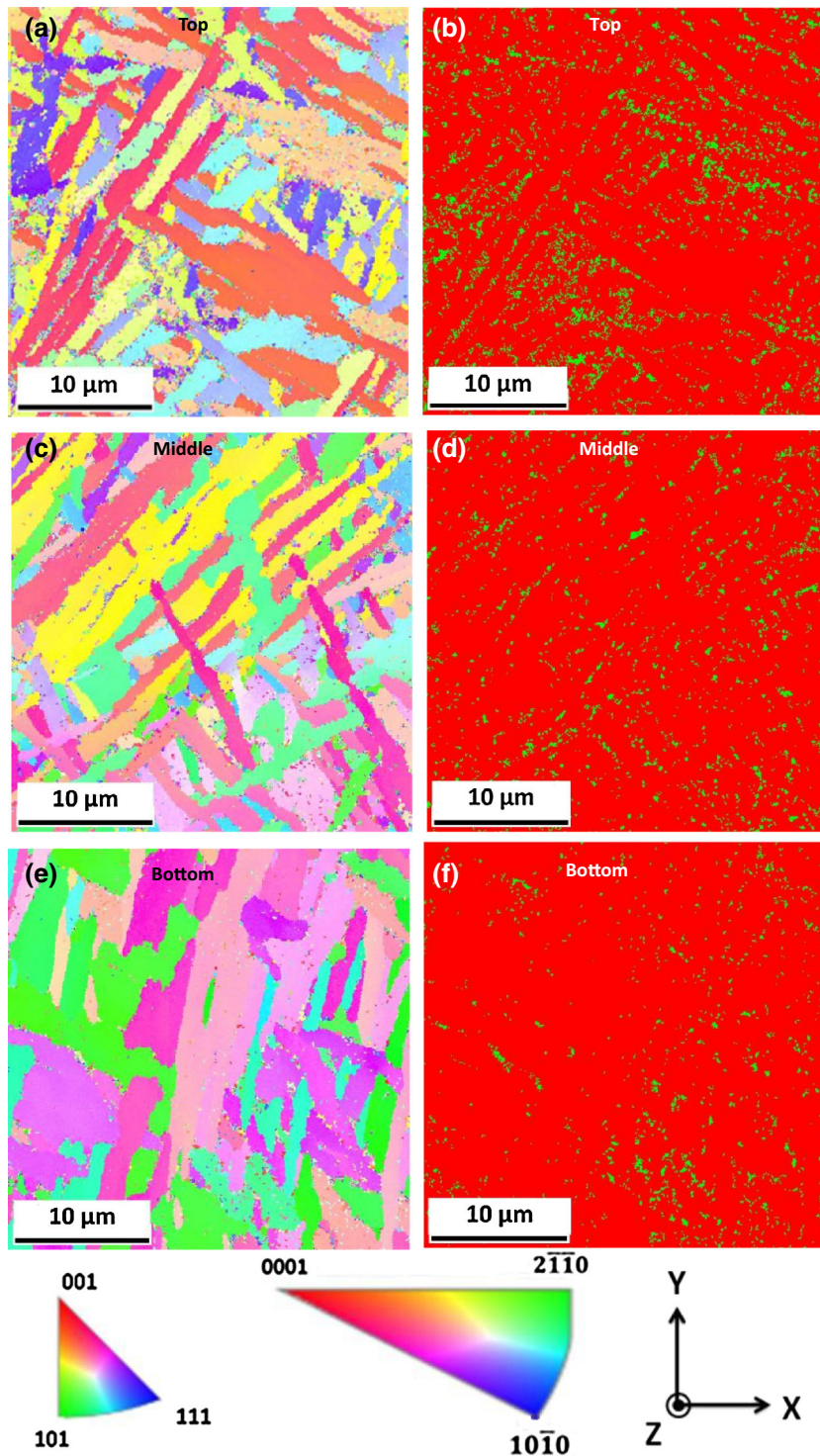


Fig. 7—EBSD mapping of representative microstructures in the top (*a, b*), middle (*c, d*) and bottom (*e, f*) segments of the as-built Ti-6Al-4V rod. The left-hand side images (*a* through *e*) are inverse pole figures (IPF), while the right-hand side images (*b* through *f*) are phase distribution images (red color for α phase, green for β phase). A 10 deg misorientation was used to distinguish two different α crystallites or plates at their boundary. Refer to Fig. 2(a) for the sample coordinate system.

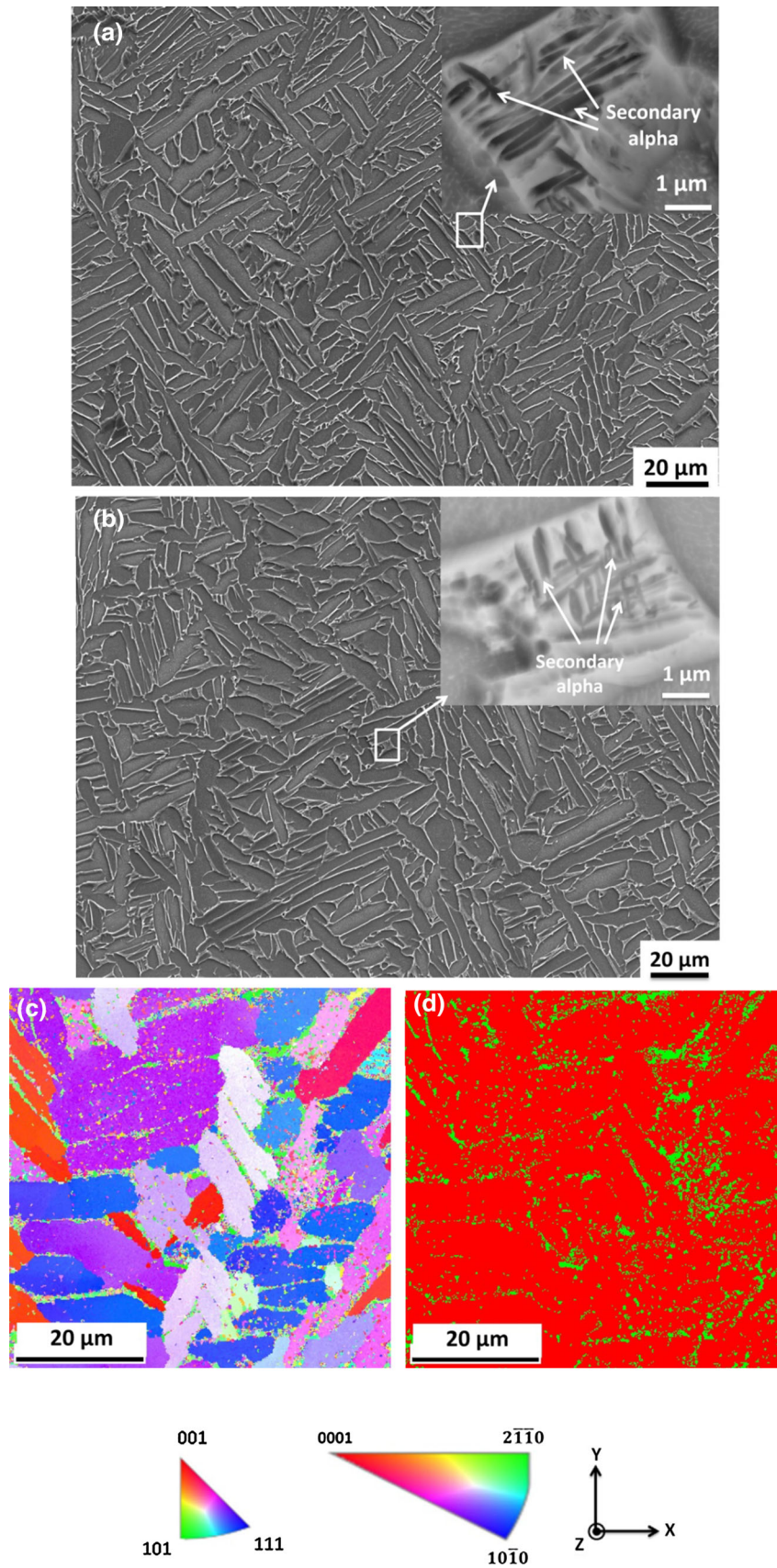


Fig. 8—SEM images and EBSD results of the Ti-6Al-4V rod after HIP. (a) and (b) are representative SEM microstructures observed in the top and bottom segments of the rod, respectively. The insets (backscattered electron images) in (a) and (b) show the precipitation of secondary α in the β phase in each microstructure. (c) is an inverse pole figures (IPF) color map and (d) is a phase distribution image (red for α and green for β).

the as-built rod (Figure 10(a)) was similar to that observed after HIP. However, the middle and bottom segments displayed different fracture features, being smaller in dimple size and less in the formation of long

tear ridges. This can be attributed to their as-built non-equilibrium inhomogeneous microstructure (see Figures 4 and 6).

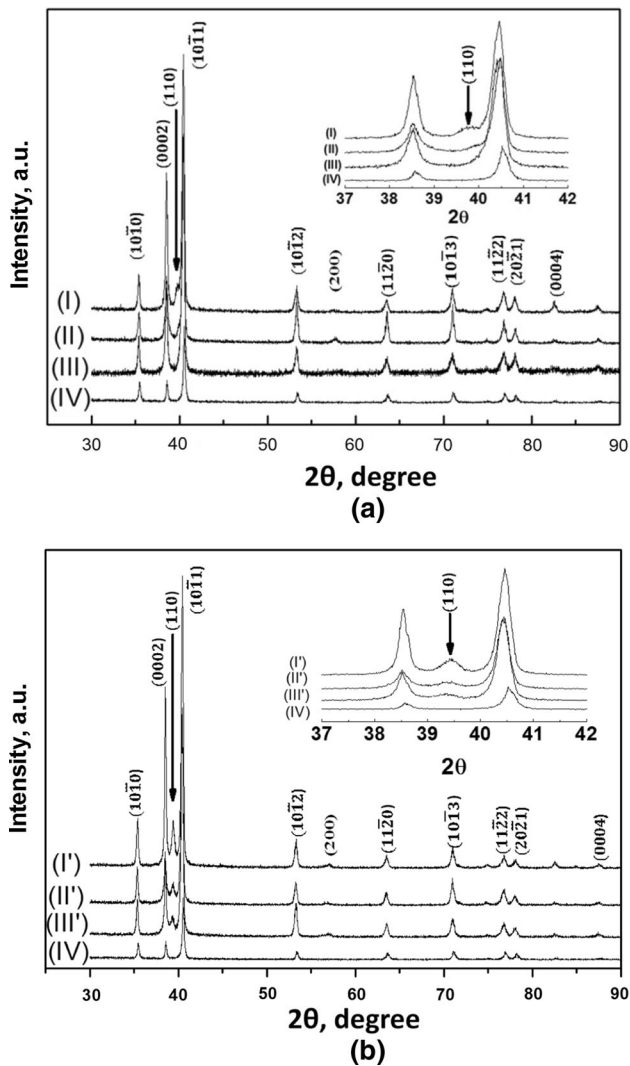


Fig. 9—XRD spectra of the top (*I, I'*), middle (*II, II'*), and bottom (*III, III'*) segments of the Ti-6Al-4V rod: (a) as-built and (b) after HIP. (*IV*) is the XRD spectrum obtained for the virgin Ti-6Al-4V powder.

IV. CONCLUSIONS

Long Ti-6Al-4V rods (diameter: 12 mm; height: 300 mm) have been additively manufactured by SEBM out of a deep powder bed and their microstructures and tensile properties were characterized both in the as-built state and after HIP. The following conclusions can be made from this study.

1. The as-built microstructure was inhomogeneous along the rod axis, where the top segment displayed the coarsest microstructure in a near equilibrium state, while the bottom segment showed the finest microstructure in a non-equilibrium state. There was a small variation (from 99.03 to 99.21 pct TD) in the relative density of the as-built Ti-6Al-4V rod. The tensile properties showed inconsistency along the rod, although they still meet the specifications set by ASTM F3001-14. In particular, the Reduction of Area decreased from (51.4 ± 2.4) to (33.9 ± 1.5) pct from the top to the bottom of the rod (the minimum requirement is 25 pct by ASTM F3001-14).
2. The inhomogeneous microstructure of the Ti-6Al-4V rod was attributed to the temperature gradient in the deep powder bed which was cooler in the bottom segment but hotter in the top segment. The temperature gradient arose from the very low thermal conductivity of the Ti-6Al-4V powder ($\leq 7 \text{ W m}^{-1} \text{ K}^{-1}$) in the powder bed and the effective heat conduction through the stainless steel substrate at the bottom of the powder bed.
3. HIP improved the relative densities of the Ti-6Al-4V rods additively manufactured by SEBM from 99.03 to 99.90 pct TD and homogenized their microstructure and therefore led to very consistent tensile properties along the rod axis.
4. For consistency and reliability, post heat treatment is needed for Ti-6Al-4V rods manufactured out of a deep powder bed by SEBM. This differs from the AM of Ti-6Al-4V samples or parts by SEBM from a shallow powder bed.

Table IV. Tensile Properties of the Ti-6Al-4V Rods Before (*i.e.*, as-Built) and After HIP

Sample Status	Sample Positions	Yield Strength (MPa)	Ultimate Tensile Strength (MPa)	Elongation (Pct)	Reduction of Area (Pct)
As-built	top	903.6 ± 24.6	991.8 ± 21.7	16.4 ± 0.8	51.4 ± 2.4
	middle	928.7 ± 13.3	1011.7 ± 14.8	13.6 ± 1.4	38.9 ± 2.8
	bottom	911.9 ± 34.3	995.5 ± 28.5	13.5 ± 0.4	33.9 ± 1.5
HIP	top	800.1 ± 12.1	909.4 ± 2.4	16.7 ± 0.8	55.8 ± 3.0
	middle	813.3 ± 14.3	908.8 ± 3.2	17.7 ± 0.9	52.0 ± 1.9
	bottom	813.9 ± 16.2	910.6 ± 4.2	16.6 ± 0.8	51.9 ± 2.5
Standard	ASTM F3001-14	795.0	860.0	10.0	25.0

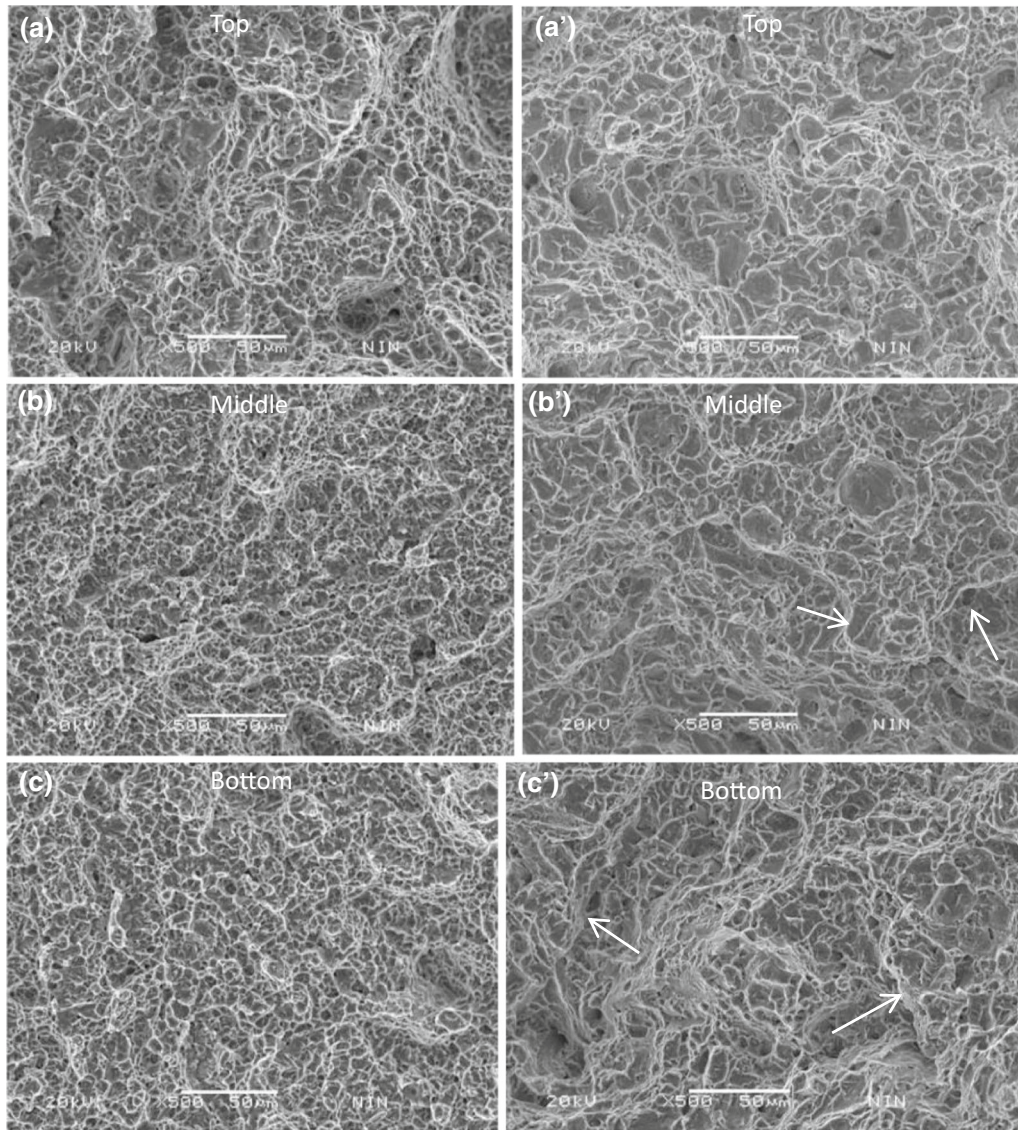


Fig. 10—Fracture surfaces of the Ti-6Al-4V rod before and after HIP. (a through c): as-built. (a' through c'): after HIP. Arrows in Fig. 10 (b'), (c') show examples of tear ridges after HIP.

ACKNOWLEDGMENTS

This work is supported in part by the International Science and Technology Cooperation Programme (2011DFA52590) of the Ministry of Science and Technology China and the Australian Research Council (ARC) through the Discovery Grant (DP120101672). Dr Bin Liu of Central South University China is acknowledged for his assistance with the EBSD work. Shenglu Lu further acknowledges the support of a visiting scholarship from the China Scholarship Council (CSC). Useful and in-depth comments and suggestions received from the reviewers are acknowledged.

REFERENCES

1. X.Y. Cheng, S.J. Li, L.E. Murr, Z.B. Zhang, Y.L. Hao, R. Yang, F. Medina, and R.B. Wicker: *J. Mech. Behav. Biomed. Mater.*, 2012, vol. 16, pp. 153–62.
2. V. Juechter, T. Scharowsky, R.F. Singer, and C. Körner: *Acta Mater.*, 2014, vol. 76, pp. 252–58.
3. H.P. Tang, M. Qian, N. Liu, X.Z. Zhang, G.Y. Yang, and J. Wang: *JOM*, 2015, vol. 67, pp. 555–63.
4. W. Xu, M. Brandt, S. Sun, J. Elambasseril, Q. Liu, K. Latham, K. Xia, and M. Qian: *Acta Mater.*, 2015, vol. 85, pp. 74–84.
5. D. Whittaker: *Powder Metall. Rev.*, 2014, vol. 3, pp. 53–59.
6. A. Safdar, L.Y. Wei, A. Snis, and Z. Lai: *Mater. Charact.*, 2012, vol. 65, pp. 8–15.
7. L.E. Murr, E.V. Esquivel, S.A. Quinones, S.M. Gaytan, M.I. Lopez, E.Y. Martinez, F. Medina, D.H. Hernandez, E. Martinez,

- J.L. Martinez, S.W. Stafford, D.K. Brown, T. Hoppe, W. Meyers, U. Lindhe, and R.B. Wicker: *Mater. Charact.*, 2009, vol. 60, pp. 96–105.
8. S.S. Al-Bermani, M.L. Blackmore, W. Zhang, and I. Todd: *Metall. Mater. Trans. A*, 2010, vol. 41A, pp. 3422–34.
 9. A.B. Arcam. Arcam Annual Report 2012. <http://www.arcam.com>. Accessed on 20 December 2014.
 10. <http://software.materialise.com/sites/default/files/public/SAM/Others/arcam.pdf> Accessed on 19 December 2014.
 11. F3001-14 A. *Standard Specification for Additive Manufacturing Titanium-6 Aluminum-4 Vanadium ELI (Extra Low Interstitial) with Powder Bed Fusion*, West Conshohocken, PA, ASTM, 2014.
 12. E8/E8M. *Standard Test Methods for Tension Testing of Metallic Materials*, West Conshohocken, PA, ASTM, 2012.
 13. G. Welsch, R. Boyer, and E.W. Collings: *Materials Properties Handbook: Titanium Alloys*, Materials Park, ASM International, 1994, p. 488.
 14. G. Lütjering and J.C. Williams: *Titanium*, 2nd ed., Springer, Berlin, 2003, pp. 42–44.